1 **Investigation of small molecule inhibitors of the SARS-CoV-2 papain-like protease by all-**

2 **atom microsecond modelling, PELE Monte Carlo simulations, and *in vitro* activity**

3 **inhibition**

4 Julia J Liang[1,2], Eleni Pitsillou[1,2], Katherine Ververis[1], Victor Guallar[3,4], Andrew Hung[2], Tom

5 C Karagiannis[1,5]

6 [1] Epigenomic Medicine, Department of Diabetes, Central Clinical School, Monash University,

7 Melbourne, VIC 3004, Australia

8 [2] School of Science, STEM College, RMIT University, VIC 3001, Australia

9 [3] Barcelona Supercomputing Center, Jordi Girona 29, E-08034 Barcelona, Spain

10 [4] ICREA, Passeig Lluís Companys 23, E-08010 Barcelona, Spain

11 [5] Department of Clinical Pathology, The University of Melbourne, Parkville, VIC 3052,

12 Australia

13

14 Keywords: Coronavirus, COVID-19, SARS-CoV-2, papain-like protease, GRL0617,

15 hypericin, molecular modelling

16 Running (short) title: SARS-CoV-2 papain-like protease inhibitors

17
18 Author for correspondence:

19 Tom Karagiannis, PhD

20 Head Epigenomic Medicine Program

21 Department of Diabetes

22 Central Clinical School

23 Monash University

24 Melbourne, VIC 3004, Australia

25 email: tom.karagiannis@monash.edu

26 phone: 61 400 857 906

**Abstract**

The SARS-CoV-2 papain-like (PL$^{pro}$) protease is essential for viral replication. We investigated potential antiviral effects of hypericin relative to the well-known noncovalent PL$^{pro}$ inhibitor GRL-0617. Molecular dynamics and PELE Monte Carlo simulations highlight favourable binding of hypericin and GRL-0617 to the naphthalene binding pocket of PL$^{pro}$. Although not potent as GRL-0617 (45.8 vs 1.6μM for protease activity, respectively), *in vitro* fluorogenic enzymatic assays with hypericin show concentration-dependent inhibition of both PL$^{pro}$ protease and deubiquitinating activities. Given its use in supplementations and the FDA conditional approval of a synthetic version, further evaluation of hypericin as a potential SARS-CoV-2 antiviral is warranted.

**Introduction**

Severe acute respiratory syndrome coronavirus 2 (SARS-CoV-2) is the highly transmissible pathogen responsible for coronavirus disease 2019 (COVID-19) and the evolving pandemic [1]. A number of SARS-CoV-2 variants of concern have been identified by the World Health Organization (WHO), and the increased transmissibility or virulence of emerging variants continues to be a challenge [2]. Upon entry into host cells, the single-stranded RNA genome (positive-sense) is released into the cytoplasm and the polyproteins pp1a and pp1ab are produced from the translation of the open reading frames (ORF1a and ORF1b) [3, 4]. The polyproteins are cleaved by two cysteine proteases, the main protease (M$^{pro}$) and papain-like protease (PL$^{pro}$), to form 16 non-structural proteins (nsps) [3, 4]. The M$^{pro}$ is located at nsp5 and the PL$^{pro}$ domain is encoded within nsp3 [3].

Cysteine proteases play an essential role in the virus life cycle and have been identified as promising drug targets [5]. The SARS-CoV-2 PL$^{pro}$ is comprised of an N-terminal ubiquitin-

like domain (Ubl), thumb domain, finger domain, and palm domain (Figure 1A). The protease activity of PL$^{pro}$ is coordinated by the conserved catalytic triad residues C111, H272, and D286 (Figure 1A) [6, 7]. The SARS-CoV-2 PL$^{pro}$ recognises the P4-P1 consensus sequence LXGG (X = any amino acid) and hydrolyses the peptide bond that is found between nsp1-nsp2, nsp2-nsp3, and nsp3-nsp4 (P4-P1↓P1') [8]. This results in the release of nsp1, nsp2, and nsp3 [8].

The immunomodulating activities of the SARS-CoV-2 PL$^{pro}$ are also being explored. Ubiquitination is a posttranslational modification that regulates cellular pathways, including immune responses to viral infections [9]. The C-terminus of ubiquitin and ubiquitin-like proteins, which carries the LXGG motif, binds to target proteins by forming a covalent isopeptide bond with the ε-amino group of lysine side chains [10]. Studies have demonstrated that the SARS-CoV and SARS-CoV-2 PL$^{pro}$ have deubiquitinating and deISGylating activities, which result in the inhibition of the antiviral immune response [10, 11]. The SARS-CoV and SARS-CoV-2 PL$^{pro}$ preferentially target ubiquitin chains and interferon-stimulated gene 15 (ISG15), respectively [6, 10-12]. Furthermore, two ubiquitin binding sites (SUb1 and SUb2) have been identified in PL$^{pro}$ and the SUb2 region facilitates the binding of K48-diubiquitin or -polyubiquitin and ISG15 [13]. In comparison to the SUb2 site, the active site and SUb1 site of the SARS-CoV and SARS-CoV-2 PL$^{pro}$ exhibit high conservation at the amino acid level [6].

Due to PL$^{pro}$ being a multifunctional protein, it is an attractive target for therapeutic agents [14]. Covalent inhibitors of the SARS-CoV-2 PL$^{pro}$, such as VIR250 and VIR251, have predominantly been designed to modify the catalytic triad residue C111 through a Michael Addition reaction and form a covalent thioether bond [6]. Ebselen, an organoselenium drug, and its analogues have also been identified as covalent inhibitors of the SARS-CoV and SARS-CoV-2 PL$^{pro}$ [15]. Moreover, noncovalent inhibitors have gained a significant amount of attention and this includes naphthalene-based compounds [16]. GRL-0617 was initially

developed as a noncovalent inhibitor of the SARS-CoV PL[pro] and has been found to inhibit the SARS-CoV-2 PL[pro] [11, 17]. The naphthalene-based inhibitor binds to the S3 and S4 subsites and is positioned in a cleft that leads to the active site [7, 8, 11, 17, 18].

Using molecular docking and enzymatic assays, we previously identified hypericin as a potential lead compound from a library of 300 ligands for the inhibition of the SARS-CoV-2 PL[pro] [19, 20]. The naphthodianthrone hypericin is a secondary metabolite found in St. John's Wort *(Hypericum perforatum)* and the broad pharmacological activities of this compound have been reported [21]. Hypericin has also been identified as a potential inhibitor against the SARS-CoV-2 M[pro] [22, 23]. The chemopreventative properties of synthetic hypericin (SGX-301) have been of particular interest and the clinical development of SGX-301 as a photosensitising agent for the treatment of cutaneous T-cell lymphoma is underway in the European Union and USA [24].

Here, our aim was to investigate the potential PL[pro] inhibition activity of hypericin relative to the well-known noncovalent inhibitor GRL-0617. We performed comparative *in silico* all-atom microsecond molecular dynamics and Protein Energy Landscape Exploration (PELE) Monte Carlo simulations to investigate the stability and interactions of hypericin and GRL-0617 with the PL[pro] naphthalene binding pocket. Further, we performed *in vitro* PL[pro] protease and deubiquitinase activity assays to determine the inhibition activity of hypericin in comparison to GRL-0617.


**Materials and Methods**

*All-atom molecular dynamics simulations*

GRL-0617, hypericin and its isomer were docked using the quantum-mechanics polarised

ligand docking (QPLD) protocol of the Schrödinger suite [25, 26] to the naphthalene binding

site of SARS-CoV-2 PL[pro] (PDB ID: 7JRN) [27] to serve as starting structures for simulations,

as previously described [20]. Briefly, a 20 x 20 x 20 Å receptor grid was centred around

residues surrounding the co-crystallised ligand. Using the QPLD docking protocol, initial

docking was carried out with the extra precision (XP) scoring function of Glide [28], and partial

charges of the ligand were calculated using quantum mechanical methods with the 'accurate'

setting in Jaguar [29]. Subsequent re-docking was performed with XP docking mode, with final

poses selected based on GlideScore. The docked GRL-0617 had an RMSD of 0.52 Å compared

to the crystal structure. SwissParam was used to generate ligand topologies [30].

Molecular dynamics (MD) simulations using GROMACS 2018.2 software [31, 32] were

performed with the CHARMM27 force field [33, 34], as previously described [23]. The TIP3P

water model [35] was used to solvate the protein-ligand complexes in a dodecahedral box with

a distance of 2.0 nm between protein atoms and the box edge. The system was neutralised with

sodium ions, and underwent energy minimisation using the steepest-descent gradient method.

Equilibration was performed with the canonical (NVT) ensembled followed by an isothermal-

isobaric ensemble (NPT) for 100 ps. A modified Berendsen thermostat [36] was used to

maintain a temperature of 310 K, and pressure at 1.0 bar the Parrinello-Rahman barostat [37].

The LINCS algorithm [38] was applied to constrain bond lengths, particle-mesh Ewald scheme

(PME) [39] was used to calculate long-range electrostatic forces (grid spacing 0.16 nm), and

cut-off ratios for Coulomb and van der Waals potentials were set at 1.2 nm. Production runs

were carried out for 1000 ns with a time-step of 2 fs. Additional simulations were performed

for 100 ns in triplicate.

Simulated trajectories were visualised and analysed using Visual Molecular Dynamics 1.9.3

[40] and PyMOL [41]. Analysis tools included within the GROMACS software package were

utilised, including gmx rms and gmx rmsf for calculation of RMSD and RMSF for the protein backbone. Clusters of similar structures based on RMSD of the protein backbone were calculated for the entire trajectory using gmx cluster, utilising the gromos clustering algorithm as described by Daura et al. [42]. An RMSD cut-off of 0.2 nm was used to define two structures as neighbours to obtain approximately 32 clusters for each system. The central structure of each cluster was written for analysis. The number of contacts between residues of PL[pro] and the ligands was calculated using gmx mindist with a threshold of 0.45 nm to define a contact [31, 32]. This was calculated as an average number between the ligand and each residue throughout the entire trajectory.

*PELE Monte Carlo energy landscape explorations*

Protein energy landscape exploration (PELE) analysis was performed as described previously [23, 43]. Briefly, binding sites for GRL-0617 and hypericin were identified on the SARS-CoV-2 PL[pro] using an adaptive-PELE Monte Carlo (MC) search. This involves random placement of fully solvated ligands with no direct contact with the protein (40 initial positions) to undertake an unsupervised global search and local refinement of binding sites along the entire protein surface [43]. The process involves approximately 256,000 PELE steps to provide 100 epochs, or rounds, of 10 Monte Carlo steps using 256 computing cores for global sampling of combined large (~3 Å) and short (~1 Å) ligand translations [43].

Following the global search, the best poses from local minima with lower interaction energy were used to define initial structures for local refinement. Local refinement was performed with shorter simulations involving smaller ligand translations and rotations; 10 epochs of 24 MC steps (20-30 computing cores per minima). The integrated PELE protein-ligand interaction energy was calculated for analysis by subtracting the receptor and ligand energies from the

1　complex at a given geometry, using the OPLS-AA force with a generalised surface Born

2　solvent model [43]. This produced unbiased binding sites which were discriminated among the

3　GRL-0617 and hypericin ligands.

4

5　*Fluorogenic PL$^{pro}$ protease and deubiquitinase inhibition assays*

6　To investigate the inhibitory activity of small molecules *in vitro*, proprietary PL$^{pro}$ protease and

7　deubiquitinase assay kits, which contain the recombinant PL$^{pro}$ and appropriate substrates, were

8　utilised according to the manufacturer's protocols (BPS Bioscience, San Diego, CA, USA).

9　Hypericin (89%, HWI pharma services GmbH, Germany), was prepared as a 20mM stock and

10　stored at -80ºC until use.  Working stocks of hypericin were prepared by doubling dilution to

11　achieve final concentrations in the range of $1.5 - 200\mu M$. The positive internal control GRL-

12　0617 was used at final concentration of $100\mu M$. Following incubation the fluorogenic substrate

13　(excitation wavelength = 360nm) was measured at 460nm using a CLARIOstar microplate

14　reader (BMG Labtech, Ortenberg, Germany), at gains of 1164 and 1460 for the protease and

15　deubiquitinase assays, respectively, to ensure that both background and test values were in an

16　appropriate range for accurate detection. In both assays, the test inhibitors were assayed in

17　triplicate; six determinations were made for the background and nine for total PL$^{pro}$ protease

18　and deubiquitinase activities and the GRL-0617 positive control.  Absolute fluorescence

19　intensity values at 460 nm were measured, and % protease inhibition activity at $100\mu M$

20　hypericin and GRL0617, and IC$_{50}$ values for hypericin were calculated.

21

22　**Results and Discussion**

23　*Structural effects in response to ligand binding to the PL$^{pro}$ naphthalene binding site*

MD simulations were performed using previously identified [20] compounds GRL-0617, hypericin, and its isomer (Figure 1B) with trajectories spanning 1000 ns. Analysis of the PL$^{pro}$ trajectories show a jump in protein backbone RMSD approximately halfway through the simulation for the apo and GRL-0617-bound PL$^{pro}$ (Figure 1C). The average RMSD of apo PL$^{pro}$ went from 0.20 to 0.55 nm at 544 ns. Similarly, the RMSD of GRL-0617-bound PL$^{pro}$ jumps from 0.20 to 0.50 nm at 520 ns. Hypericin-bound PL$^{pro}$ briefly has an RMSD of 0.20 nm for the first 15 ns before maintaining an average RMSD of 0.58 nm for the remaining trajectory. Hypericin-isomer-bound PL$^{pro}$ quickly reaches equilibrium, with the trajectory maintaining a stable average RMSD of 0.22 nm after 1 ns. Triplicate 100 ns trajectories also showed that all systems reached equilibrium within 10 ns (Figure S1). The number of hydrogen bonds within the protein were similar for all systems, with averages of 236 for apo, 233 for GRL-0617-bound, and 230 for hypericin and its isomer-bound PL$^{pro}$ (Figure S2).

Similar trends are observed in cluster analysis, which show two distinct conformations of PL$^{pro}$ that dominate throughout the trajectory (Figure 2). Both the apo-PL$^{pro}$ and GRL-0617-bound PL$^{pro}$ adopt a similar conformation for the first half of the trajectory, with frames corresponding to cluster 1 structures for 41.9% and 44.5% of the trajectory in apo and GRL-0617-bound systems respectively. For the second half of the trajectory, the cluster 2 structure is dominant, with 40.4% of apo and 44.0% of GRL-0617-bound PL$^{pro}$ frames of the trajectory corresponding to this conformation. The hypericin analogue-bound PL$^{pro}$ systems adopt a single conformation for the majority of the trajectory. Hypericin-bound PL$^{pro}$ maintains the equivalent of apo and GRL-0617-bound cluster 2 conformation for 78.4% of the trajectory. Conversely, hypericin-isomer-bound PL$^{pro}$ maintains a conformation corresponding to the cluster 1 structures for apo and GRL-0617 for 82.1% of the trajectory. It is noted that this conformation is close to the crystal structure. The apo cluster 1 structure has an RMSD of 1.55 Å compared to the crystal

1 structure, whereas the cluster 2 structure has an RMSD of 5.45 Å (Table S1). The differences

2 between the structures can be attributed to the Ubl-domain (Figure S3).

3 RMSF analysis indicates the fluctuation in RMSD may be attributed to the N-terminal Ubl

4 domain of PL$^{pro}$ (Figure 1D), which demonstrated the greatest flexibility in the protein. All

5 ligands are shown to suppress RMSF, with hypericin and its isomer more effective than GRL-

6 0617, especially at the Ubl domain (Figure 1D). This is likely due to hypericin analogue-bound

7 PL$^{pro}$ systems remaining in a single cluster conformation for ~80% of the trajectory (Figure 2).

8 The blocking loop 2 (BL2, GNYQCGH) region is flexible, with these residues having a higher

9 RMSF for hypericin-bound compared to the isomer and GRL-0617-bound PL$^{pro}$. In particular,

10 Y268 had an RMSF of 0.54 nm in apo and 0.44 nm in hypericin-bound PL$^{pro}$, compared to

11 values of 0.24 and 0.26 nm in GRL-0617 and hypericin-isomer-bound PL$^{pro}$, respectively

12 (Figure 1D).

13 *Stability of compounds bound to the PL$^{pro}$ active site*

14 Visual analysis of trajectories indicates a largely stable enzyme with contraction and expansion

15 of the Ubl domain corresponding to conformational changes described by changes in RMSD

16 and cluster analysis (Movies S1 to S4). GRL-0617 stays firmly bound to the naphthalene

17 binding site throughout the trajectory (Movie S2), reinforcing its validity as a positive control.

18 Contacts analysis demonstrates the proximity of the ligand with key residues in the naphthalene

19 binding pocket (Figure 3), particularly Y268 which had an average of 107 contacts with GRL-

20 0617 throughout the trajectory. Also prominent was D164 (65 contacts) and P248 (69 contacts).

21 Analysis of hydrogen bonds indicates that GRL-0617 demonstrated a greater average number

22 of hydrogen bonds were formed with PL$^{pro}$, forming an average of 2.34 hydrogen bonds with

23 PL$^{pro}$, compared with values of 0.76 and 0.83 for hypericin and its isomer (Figure S2).

24 Similarly, the isomer of hypericin also remained bound to the naphthalene binding pocket for

the duration of the trajectory (Movie S4), forming contacts with similar residues. Y268 is the

most frequent residue, forming an average of 139 contacts with the hypericin isomer

throughout the trajectory. Contacts were also formed between the hypericin isomer and

residues located deeper within the binding site, including R166 (65 contacts) and M208 (16

contacts) (Figure 3).

While ligand unbinding was initially observed, hypericin re-attaches to the enzyme at

approximately 150 ns into the trajectory at the active site of the enzyme in proximity to the

catalytic triad residues (Movie S3). This is also illustrated in Figure S4 depicting the distance

between ligands and the catalytic triad residues throughout the trajectory. Hypericin initially

deviates from the naphthalene binding site before binding to the active site of PL$^{pro}$, with an

average distance of 0.95 nm from the catalytic triad residues after 150 ns. This is closer than

GRL-0617 and the hypericin isomer, which were 1.38 and 1.61 nm from the catalytic triad

residues, respectively (Figure S4).  While modest, contacts are observed between hypericin

and the catalytic C111, H272 and D286 residues (Figure 3). The most frequent residue in

contact with hypericin throughout the trajectory was W106 (127 contacts). Although hypericin

was binding to a different site to its isomer and GRL-0617, Y268 is still among the most

prominent residues, forming an average of 96 contacts with hypericin. This residue is located

within the BL2 loop, which ordinarily caps the naphthalene binding site [7], but in this case is

flipped downwards to an open conformation, accommodating binding of hypericin with the

catalytic residues in the active site. This is supported by the higher RMSF of Y268 (Figure 1D)

for hypericin-bound PL$^{pro}$, as well as the RMSD observed for BL2 loop residues (Figure S5).

The RMSD of BL2 loop residues remain relatively stable for GRL-0617 and hypericin isomer-

bound PL$^{pro}$, with average values of 0.25 and 0.42 nm for the entire trajectory, respectively.

The ligand-free PL$^{pro}$ shows the BL2 loop flipping open and closed for the first 400 ns, before

remaining closed to cap the naphthalene binding site for the remainder of the trajectory with

1 an average RMSD of 0.22 nm (Figure S5). This may indicate that as well as capping the

2 naphthalene binding site, the BL2 loop functions to secure ligand binding to the active site.

3 This suggests a ligand-mediated induced-fit mechanism which prevents the binding of natural

4 LXGG motif-containing substrates, resulting in the inhibition of both the protease and

5 deubiquitinase activities of PL$^{pro}$ [7, 17, 44].

6

7 *PELE Monte Carlo simulations highlight ligand interactions with PL$^{pro}$ binding pockets*

8 Adaptive-PELE Monte Carlo simulations were performed with GRL-0617 and hypericin to

9 identify binding modes on PL$^{pro}$. The plot in Figure 4 depicts all the interaction energies for

10 poses explored by PELE against the RMSD to the initial crystal structure of GRL-0617. Only

11 using the crystal structure as analysis, the best protein-ligand poses with the lowest interaction

12 energies were located in the naphthalene binding site (Figure 4A). These poses are at 1 Å and

13 3 Å from the crystal structure, producing binding affinities of -38 and -39 kcal/mol,

14 respectively, with residue interactions similar to that of the co-crystallised GRL-0617 (Figure

15 4C). This shows that PELE reproduces the crystal structure.

16 Hypericin was also found to bind to the naphthalene binding site, with pose 1 (Figure 5)

17 producing a binding affinity of -47 kcal/mol. As well as the naphthalene binding pocket,

18 additional binding sites were identified for hypericin. Notably, pose 2 (Figure 5) was near the

19 catalytic triad residues, positioned in a similar manner to hypericin following MD simulation

20 (Figure 3, Movie S3). This pose had a binding affinity of -46 kcal/mol, forming hydrogen bonds

21 with N109, C270, L274, and the catalytic D286. Additional poses were identified with

22 comparable binding energies: pose 3 between the palm and thumb domains (-53 kcal/mol) and

23 pose 5 located on the Ubl-like domain (-48 kcal/mol). Pose 4 (-51 kcal/mol) was in the zinc

24 finger domain, forming a hydrogen bond with the zinc-coordinating residue C189 (Figure 5C).

1. This residue has been targeted for inhibition with other small molecules to disrupt zinc binding

2. in SARS-CoV-2 PL$^{pro}$ [45]. Overall these findings indicate that hypericin preferentially binds

3. to the canonical naphthalene binding and active sites associated with inhibition of the PL$^{pro}$,

4. and also may possess zinc-modifying properties [45].

5.

6. *Hypericin inhibits the SARS-CoV-2 PL$^{pro}$ protease and deubiquitinase activities <u>in vitro</u>*

7. We have previously investigated the in vitro PL$^{pro}$ protease and deubiquitinase inhibitory

8. activities of small molecules including those of hypericin [19, 20]. Here, our findings confirm

9. the concentration-dependent inhibition of PL$^{pro}$ protease and deubiquitinase activities of

10. hypericin (Figure 6). At a concentration of 100μM, hypericin possessed inhibition activities

11. (97.9 ± 1.8 and 91.4 ± 3.2 for protease and deubiquitinase, respectively), that were analogous

12. to the internal positive control GRL-0617 (96.9 ± 1.6μM and 88.4 ± 4.9μM; Table 1). However,

13. the IC$_{50}$ values were calculated to be 45.8 ± 7.2μM and 20.3 ± 8.3μM for the PL$^{pro}$ protease

14. and deubiquitinase inhibition activities of hypericin, highlighting decreased potency compared

15. to GRL-0617 (1.6μM and 1.7μM; Table 1). Typical plasma concentrations of hypericin range

16. from 36 − 180 nM following consumption of LI 160 hypericum extracts containing 1.09 − 4.36

17. mg hypericin [46]. Standard over the counter formulations of St John's wort contain

18. approximately 1 mg of hypericin. It is noteworthy that it has been used in a variety of human

19. clinical trials, including in the context of premenstrual syndrome, nonmelanoma skin cancer,

20. and hepatitis C virus infection [47-49]. Furthermore, concentration-dependent uptake of

21. hypericin has been observed in Caco-2 cell assays [50]. Nevertheless, the inhibition activities

22. are within biologically relevant ranges and the findings are encouraging.

23.

## Conclusion

Overall, microsecond molecular dynamics simulations highlight the stability of GRL-0617 and hypericin in the naphthalene binding pocket of the SARS-CoV-2 PL$^{pro}$. Similarly, PELE Monte Carlo simulations indicate favourable energies associated with interactions of the small molecules in the naphthalene binding site. Finally, enzymatic assays *in vitro* confirm the potency with respect to inhibition of PL$^{pro}$ protease and deubiquitinase activities of the well-known inhibitor GRL-0617. In comparison, although not as potent, hypericin also inhibits PL$^{pro}$ protease and deubiquitinase activities with IC$_{50}$ values in the biologically relevant micromolar range. When considering potential clinical utility, the long history of use of hypericin in supplementations and the conditional Food and Drug Administration (FDA) approval of a synthetic version (designated SGX 301), are encouraging, and highlight the importance of further evaluation in appropriate antiviral models.

## Author contributions statement

TCK, AH, and VG conceptualized the aims and methodology, were involved in supervision, and production of the first draft of the manuscript. VG performed data analysis and curated data. KV performed and analysed the *in vitro* protease inhibition assay. JJL and EP were involved in data analysis and curation, and in production of the first draft of the manuscript. All authors contributed to editing and reviewing the manuscript.

## Acknowledgements

**Conflict of interest**

Epigenomic Medicine Program (TCK) is supported financially by McCord Research (Iowa, USA), which may have a financial interest in dietary compounds described in this work. However, there is no conflict of interest with respect to the inhibition of the SARS-CoV-2 papain-like protease. The remaining co-authors also have no conflicts of interest.

**References**

1. Gorbalenya, A.E., et al., *The species Severe acute respiratory syndrome-related coronavirus: classifying 2019-nCoV and naming it SARS-CoV-2.* Nature Microbiology, 2020. **5**(4): p. 536-544.
2. Krause, P.R., et al., *SARS-CoV-2 Variants and Vaccines.* New England Journal of Medicine, 2021. **385**(2): p. 179-186.
3. V'kovski, P., et al., *Coronavirus biology and replication: implications for SARS-CoV-2.* Nature Reviews Microbiology, 2021. **19**(3): p. 155-170.
4. Khailany, R.A., M. Safdar, and M. Ozaslan, *Genomic characterization of a novel SARS-CoV-2.* Gene Reports, 2020. **19**: p. 100682.
5. Verma, S., R. Dixit, and K.C. Pandey, *Cysteine Proteases: Modes of Activation and Future Prospects as Pharmacological Targets.* 2016. **7**(107).
6. Rut, W., et al., *Activity profiling and crystal structures of inhibitor-bound SARS-CoV-2 papain-like protease: A framework for anti–COVID-19 drug design.* Science Advances, 2020. **6**(42): p. eabd4596.

7.  Gao, X., et al., *Crystal structure of SARS-CoV-2 papain-like protease*. Acta Pharmaceutica Sinica B, 2021. **11**(1): p. 237-245.

8.  Osipiuk, J., et al., *Structure of papain-like protease from SARS-CoV-2 and its complexes with non-covalent inhibitors*. Nature Communications, 2021. **12**(1): p. 743.

9.  Gu, H. and B. Jan Fada, *Specificity in Ubiquitination Triggered by Virus Infection*. International journal of molecular sciences, 2020. **21**(11): p. 4088.

10. Ratia, K., et al., *Structural Basis for the Ubiquitin-Linkage Specificity and deISGylating Activity of SARS-CoV Papain-Like Protease*. PLOS Pathogens, 2014. **10**(5): p. e1004113.

11. Shin, D., et al., *Papain-like protease regulates SARS-CoV-2 viral spread and innate immunity*. Nature, 2020. **587**(7835): p. 657-662.

12. Drag, M., et al., *Positional-scanning fluorigenic substrate libraries reveal unexpected specificity determinants of DUBs (deubiquitinating enzymes)*. The Biochemical journal, 2008. **415**(3): p. 367-375.

13. Klemm, T., et al., *Mechanism and inhibition of the papain-like protease, PLpro, of SARS-CoV-2*. The EMBO Journal, 2020. **39**(18): p. e106275.

14. McClain, C.B. and N. Vabret, *SARS-CoV-2: the many pros of targeting PLpro*. Signal Transduction and Targeted Therapy, 2020. **5**(1): p. 223.

15. Weglarz-Tomczak, E., et al., *Identification of ebselen and its analogues as potent covalent inhibitors of papain-like protease from SARS-CoV-2*. Scientific Reports, 2021. **11**(1): p. 3640.

16. Delre, P., et al., *Repurposing Known Drugs as Covalent and Non-covalent Inhibitors of the SARS-CoV-2 Papain-Like Protease*. 2020. **8**(1032).

17. Ratia, K., et al., *A noncovalent class of papain-like protease/deubiquitinase inhibitors blocks SARS virus replication*. Proceedings of the National Academy of Sciences of the United States of America, 2008. **105**(42): p. 16119-16124.

18. Fu, Z., et al., *The complex structure of GRL0617 and SARS-CoV-2 PLpro reveals a hot spot for antiviral drug discovery*. Nature communications, 2021. **12**(1): p. 488-488.

19. Pitsillou, E., et al., *Identification of Small Molecule Inhibitors of the Deubiquitinating Activity of the SARS-CoV-2 Papain-Like Protease: in silico Molecular Docking Studies and in vitro Enzymatic Activity Assay*. Frontiers in chemistry, 2020. **8**: p. 623971-623971.

20. Pitsillou, E., et al., *Interaction of small molecules with the SARS-CoV-2 papain-like protease: In silico studies and in vitro validation of protease activity inhibition using an enzymatic inhibition assay*. J Mol Graph Model, 2021. **104**: p. 107851.

21. Jendželovská, Z., et al., *Hypericin in the Light and in the Dark: Two Sides of the Same Coin*. 2016. **7**(560).

22. Loschwitz, J., et al., *Novel inhibitors of the main protease enzyme of SARS-CoV-2 identified via molecular dynamics simulation-guided in vitro assay*. Bioorganic Chemistry, 2021. **111**: p. 104862.

23. Liang, J., et al., *Small molecule interactions with the SARS-CoV-2 main protease: In silico all-atom microsecond MD simulations, PELE Monte Carlo simulations, and determination of in vitro activity inhibition*. Journal of Molecular Graphics and Modelling, 2022. **110**: p. 108050.

24. Scarisbrick, J.J., M. Bagot, and P.L. Ortiz-Romero, *The changing therapeutic landscape, burden of disease, and unmet needs in patients with cutaneous T-cell lymphoma*. British journal of haematology, 2021. **192**(4): p. 683-696.

25. Schrödinger, *Schrödinger Release 2020-2: QM-Polarized Ligand Docking protocol; Glide, Schrödinger, LLC, New York, NY, 2016; Jaguar, Schrödinger, LLC, New York, NY, 2016; QSite, Schrödinger, LLC, New York, NY, 2020*. 2020.

26.  Cho, A.E., et al., *Importance of accurate charges in molecular docking: quantum mechanical/molecular mechanical (QM/MM) approach.* Journal of computational chemistry, 2005. **26**(9): p. 915-931.

27.  Ma, C., et al., *Discovery of SARS-CoV-2 Papain-like Protease Inhibitors through a Combination of High-Throughput Screening and a FlipGFP-Based Reporter Assay.* ACS Cent Sci, 2021. **7**(7): p. 1245-1260.

28.  Friesner, R.A., et al., *Extra Precision Glide: Docking and Scoring Incorporating a Model of Hydrophobic Enclosure for Protein−Ligand Complexes.* Journal of Medicinal Chemistry, 2006. **49**(21): p. 6177-6196.

29.  Bochevarov, A.D., et al., *Jaguar: A high-performance quantum chemistry software program with strengths in life and materials sciences.* International Journal of Quantum Chemistry, 2013. **113**(18): p. 2110-2142.

30.  Zoete, V., et al., *SwissParam: a fast force field generation tool for small organic molecules.* J Comput Chem, 2011. **32**(11): p. 2359-68.

31.  Berendsen, H.J.C., D. van der Spoel, and R. van Drunen, *GROMACS: A message-passing parallel molecular dynamics implementation.* Computer Physics Communications, 1995. **91**(1): p. 43-56.

32.  Abraham, M.J., et al., *GROMACS: High performance molecular simulations through multi-level parallelism from laptops to supercomputers.* SoftwareX, 2015. **1-2**: p. 19-25.

33.  Bjelkmar, P., et al., *Implementation of the CHARMM Force Field in GROMACS: Analysis of Protein Stability Effects from Correction Maps, Virtual Interaction Sites, and Water Models.* Journal of Chemical Theory and Computation, 2010. **6**(2): p. 459-466.

34.  Vanommeslaeghe, K., et al., *CHARMM General Force Field (CGenFF): A force field for drug-like molecules compatible with the CHARMM all-atom additive biological force fields.* Journal of computational chemistry, 2010. **31**(4): p. 671-690.

35.  Jorgensen, W.L., et al., *Comparison of simple potential functions for simulating liquid water.* The Journal of chemical physics, 1983. **79**(2): p. 926-935.

36.  Berendsen, H.J.C., et al., *Molecular dynamics with coupling to an external bath.* The Journal of Chemical Physics, 1984. **81**(8): p. 3684-3690.

37.  Parrinello, M. and A. Rahman, *Crystal Structure and Pair Potentials: A Molecular-Dynamics Study.* Physical Review Letters, 1980. **45**(14): p. 1196-1199.

38.  Hess, B., et al., *LINCS: a linear constraint solver for molecular simulations.* Journal of computational chemistry, 1997. **18**(12): p. 1463-1472.

39.  Darden, T., D. York, and L. Pedersen, *Particle mesh Ewald: An N·log(N) method for Ewald sums in large systems.* The Journal of Chemical Physics, 1993. **98**(12): p. 10089-10092.

40.  Humphrey, W., A. Dalke, and K. Schulten, *VMD: visual molecular dynamics.* J Mol Graph, 1996. **14**(1): p. 33-8, 27-8.

41.  Schrodinger, LLC, *The PyMOL Molecular Graphics System, Version 1.8.* 2015.

42.  Daura, X., et al., *Peptide Folding: When Simulation Meets Experiment.* Angewandte Chemie International Edition, 1999. **38**(1- 2): p. 236-240.

43.  Lecina, D., J.F. Gilabert, and V. Guallar, *Adaptive simulations, towards interactive protein-ligand modeling.* Scientific Reports, 2017. **7**(1): p. 8466.

44.  Bosken, Y.K., et al., *Insights Into Dynamics of Inhibitor and Ubiquitin-Like Protein Binding in SARS-CoV-2 Papain-Like Protease.* 2020. **7**(174).

45.  Sargsyan, K., et al., *Multi-targeting of functional cysteines in multiple conserved SARS-CoV-2 domains by clinically safe Zn-ejectors.* Chemical Science, 2020. **11**(36): p. 9904-9909.

46. Brockmöller, J., et al., *Hypericin and pseudohypericin: pharmacokinetics and effects on photosensitivity in humans.* Pharmacopsychiatry, 1997. **30 Suppl 2**: p. 94-101.

47. Jacobson, J.M., et al., *Pharmacokinetics, safety, and antiviral effects of hypericin, a derivative of St. John's wort plant, in patients with chronic hepatitis C virus infection.* Antimicrobial agents and chemotherapy, 2001. **45**(2): p. 517-524.

48. Canning, S., et al., *The Efficacy of Hypericum perforatum (St John's Wort) for the Treatment of Premenstrual Syndrome.* CNS Drugs, 2010. **24**(3): p. 207-225.

49. Kacerovská, D., et al., *Photodynamic Therapy of Nonmelanoma Skin Cancer with Topical Hypericum perforatum Extract—A Pilot Study.* Photochemistry and Photobiology, 2008. **84**(3): p. 779-785.

50. Verjee, S., et al., *Permeation characteristics of hypericin across Caco-2 monolayers in the presence of single flavonoids, defined flavonoid mixtures or Hypericum extract matrix.* J Pharm Pharmacol, 2019. **71**(1): p. 58-69.

**Figure legends**

**Figure 1: Classical MD simulation of ligands bound with SARS-CoV-2 PL$^{pro}$.** A) The SARS-CoV-2 PL$^{pro}$ is composed of four main domains; the Ubl, thumb, fingers, and palm domain. PL$^{pro}$ also contains four subsites highlighted in surface representation: S1 and S2 for ubiquitin- and ISG16-binding, and naphthalene-based inhibitors bind in the S3 and S4 subsites. Protease activity is mediated by catalytic triad residues in the active site. B) Chemical structures of GRL-0617, hypericin, and its isomer. C) MD simulations were performed for 1000 ns. Root mean square deviation (RMSD) of PL$^{pro}$ protein backbone. D) Root mean square fluctuation (RMSF) of PL$^{pro}$ backbone throughout the trajectory. Data for the apo PL$^{pro}$ is shown in grey, GRL-0617-bound in red, hypericin-bound in blue, and hypericin-isomer-bound in green.

**Figure 2: Cluster analysis of 1000 ns MD simulation trajectories of SARS-CoV-2 PL$^{pro}$ complexes.** A) Heatmap depicting cluster number throughout the trajectory. The top six clusters from 100,000 frames are depicted for each system. B) Structures from different systems similar to cluster 1 of apo PL$^{pro}$, with the proportion of frames shown as a percentage. C) Structures from different systems similar to cluster 2 of apo PL$^{pro}$, with the proportion of

frames shown as a percentage. Structures for the apo PL$^{pro}$ are shown in grey, GRL-0617-bound in red, hypericin-bound in blue, and hypericin-isomer-bound in green.

**Figure 3: Number of contacts between residues of SARS-CoV-2 PL$^{pro}$ and bound ligands.** The average number of contacts throughout the trajectory between all residues of PL$^{pro}$ and bound ligands was calculated for A) GRL-0617, B) hypericin, and C) the isomer of hypericin. Residue interactions are shown for the final frame of the trajectory. Data for the GRL-0617-bound PL$^{pro}$ is shown in red, hypericin-bound in blue, and hypericin-isomer-bound in green.

**Figure 4: PELE binding site search of GRL-0617 on SARS-CoV-2 PL$^{pro}$.** A) Interaction energy plot vs RMSD distance to the crystallographic position GRL-0617 in the naphthalene binding site. The global search is shown in dark blue and structures of the first epoch are shown in cyan, showing that initial positions are not close to the crystal structure. B) The two best poses following global refinement of GRL-0617 are numbered. C) Residue interactions for co-crystallised GRL-0617, and poses identified following PELE analysis. Hydrogen bonds are depicted as dashed blue lines.

**Figure 5: PELE binding site search of hypericin on SARS-CoV-2 PL$^{pro}$.** A) Interaction energy plot vs RMSD distance to initial position of hypericin in the naphthalene binding site. The global search is shown in dark blue and locally refined poses are shown in cyan. B) The best five poses following local refinement of hypericin are numbered. C) Residue interactions for poses identified following PELE analysis. Hydrogen bonds are depicted as dashed blue lines.

**Figure 6: Inhibition of the SARS-CoV-2 PL$^{pro}$ protease and deubiquitinase activities by hypericin.** The protease and deubiquitinase inhibition activities of hypericin were determined using commercial PL$^{pro}$ assay kits, consisting of a proprietary fluorogenic substrate at an emission wavelength of 460nm (BPS Bioscience, San Diego, CA, USA). Hypericin (0.2 μM

1  to 200 μM concentration range was investigated), resulted in a concentration-dependent

2  inhibition of both protease (A), and deubiquitinase (B) activities.  Average values ± SEM from

3  triplicate determinations are shown.  The average background (n=6), total PL$^{pro}$ protease and

4  deubiquitinase activities (n=9), and inhibition by the positive control GRL-0617 at 100μM

5  (n=9), are highlighted (horizontal dotted lines).

6  **Table 1: Inhibition of PL$^{pro}$ protease and deubiquitinase activities by GRL-0617 and**

7  **hypericin.** Percentage inhibition at a ligand concentration of 100μM and IC$_{50}$ values from *in*

8  *vitro* fluorogenic PL$^{pro}$ protease and deubiquitinase assays.

9

10

1    **Supplementary Materials**

2    **Figure S1:** Average RMSD (A) and RMSF (B) SARS-Cov-2 PL$^{pro}$ backbone 100 ns

3    trajectories in triplicate. Data for apo PL$^{pro}$ is shown in grey, GRL-0617-bound in red,

4    hypericin-bound in blue, and hypericin-isomer-bound PL$^{pro}$ in green.

5    **Figure S2:** Number of hydrogen bonds for SARS-CoV-2 PL$^{pro}$ protein bound with ligands (A)

6    and protein-ligand (B), shown as mean ± SD over a 1000 ns trajectory.

7    **Figure S3:** Per-residue RMSD of backbone comparison between SARS-CoV-2 PL$^{pro}$ cluster

8    structures. A) Comparison between cluster 1 and cluster 2 structures for apo- and GRL-0617-

9    bound PL$^{pro}$. B) Comparison to cluster 1 structure of apo-PL$^{pro}$ for GRL-0617- and hypericin-

10   isomer-bound PL$^{pro}$ cluster 1. C) Comparison to cluster 2 structure of apo-PL$^{pro}$ for GRL-0617

11   cluster 2 and hypericin-bound PL$^{pro}$ cluster 1. RMSD for apo-PL$^{pro}$ is shown in grey, GRL-

12   0617- in red, hypericin isomer- in green, and hypericin-bound PL$^{pro}$ in blue.

13   **Figure S4:** Distance between the centre of mass of SARS-COV-2 PL$^{pro}$ catalytic triad residues

14   (C111, H272, D286) and bound ligands GRL-0617 (red), hypericin (blue) and its isomer

15   (green) throughout the simulation.

16   **Figure S5:** RMSD of blocking loop 2 residues (GNYQCGH) of SARS-CoV-2 PL$^{pro}$ over 1000

17   ns. Data for apo PL$^{pro}$ is shown in grey, GRL-0617-bound in red, hypericin-bound in blue, and

18   hypericin-isomer-bound PL$^{pro}$ in green.

19   **Table S1:** RMSD alignment in angstroms (Ǻ) of SARS-CoV-2 PL$^{pro}$ backbone between

20   different cluster structures, with a cut-off of 2.0 Ǻ to define a cluster

21   **Movie S1:** 1000 ns trajectory of the apo form of SARS-CoV-2 PL$^{pro}$

22   **Movie S2:** 1000 ns trajectory of GRL-0617 bound to SARS-CoV-2 PL$^{pro}$

1    **Movie S3:** 1000 ns trajectory of hypericin bound to SARS-CoV-2 PL$^{pro}$

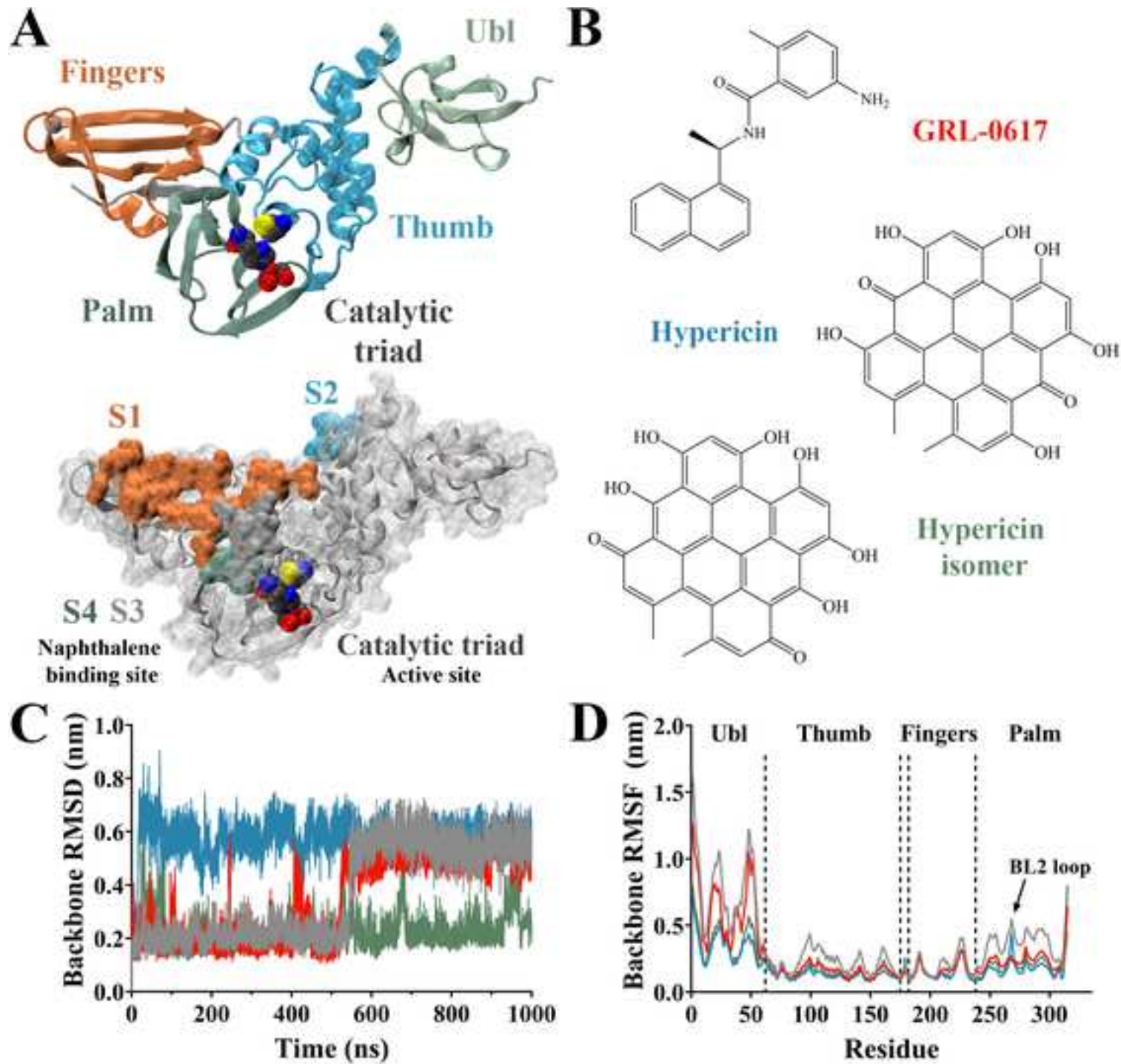2    **Movie S4:** 1000 ns trajectory of hypericin isomer bound to SARS-CoV-2 PL$^{pro}$

**Table 1: Inhibition of PL$^{pro}$ protease and deubiquitinase activities by GRL-0617 and hypericin.** Percentage inhibition at a ligand concentration of 100μM and IC$_{50}$ values from *in vitro* fluorogenic PL$^{pro}$ protease and deubiquitinase assays.
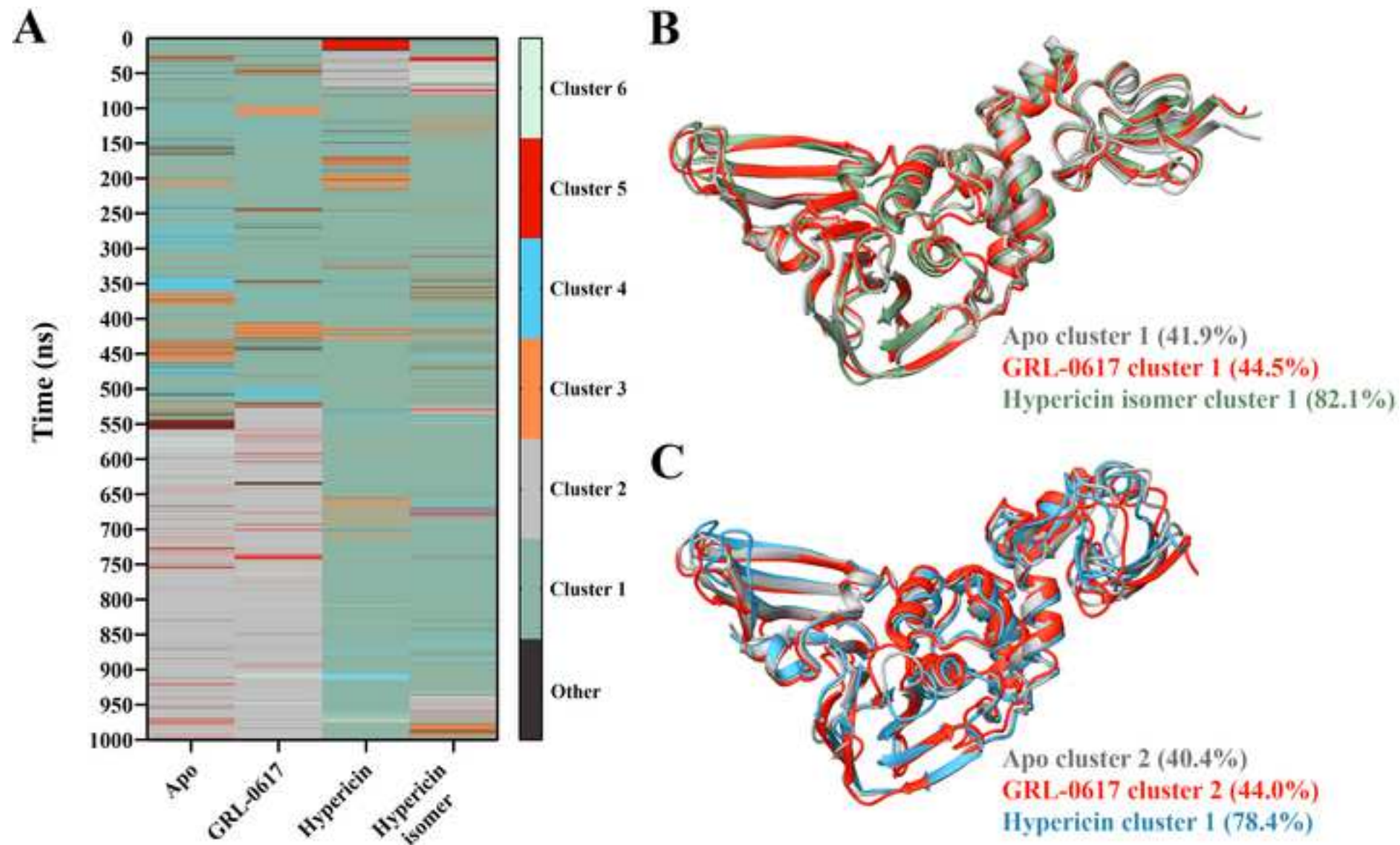
| | Protease Activity | | Deubiquitinase activity | |
|---|---|---|---|---|
| | IC$_{50}$* | % Inhibition (100μM) | IC$_{50}$* | % Inhibition (100μM) |
| **GRL-0617** | 1.6 | 96.9 ± 1.6 | 1.7 | 88.4 ± 4.9 |
| **Hypericin** | 45.8 ± 7.2 | 97.9 ± 1.8 | 20.3 ± 8.3 | 91.4 ± 3.2 |

* IC$_{50}$ values for GRL0617 according to assay manufacturer (BPS Bioscience, San Diego, CA, USA). Experimental average ± SEM indicated for hypericin (IC$_{50}$), and % inhibition at 100μM ligand concentration for GRL-0617 and hypericin.
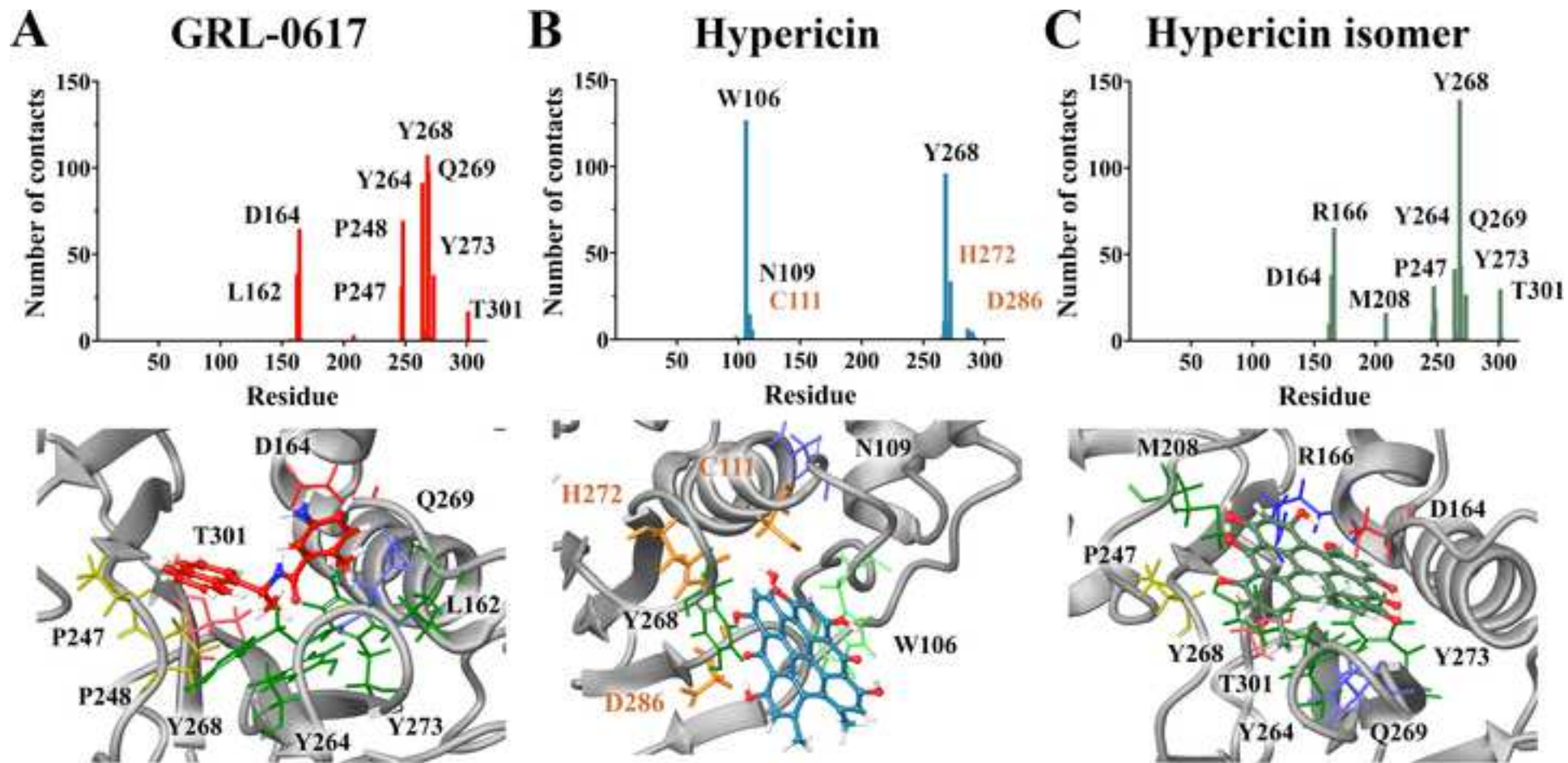
Figure 1: Classical MD simulation of ligands bound with SARS-CoV-2 PLpro. A) The
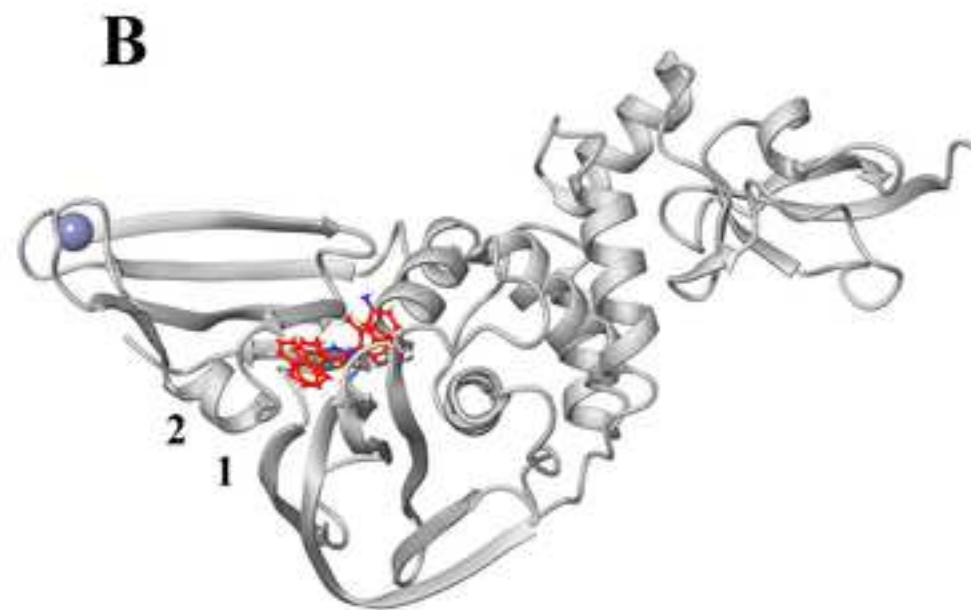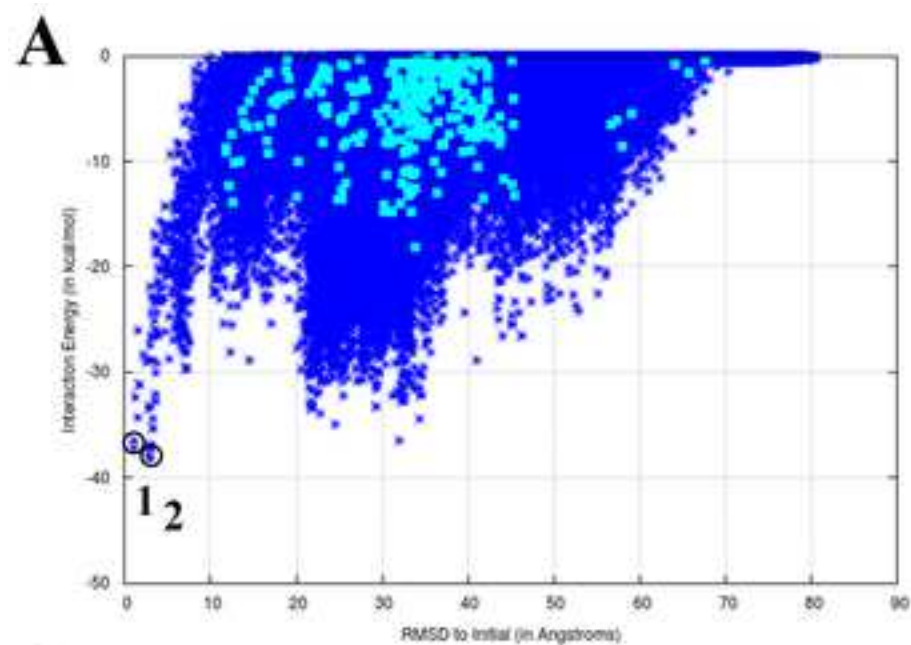SARS-CoV-2 PLpro is composed of four main domains; the Ubl, thumb, fingers, and

Click here to access/download;Figure;Figure 1 - MD PLPro_revised.tif ⬇

Figure 2: Cluster analysis of 1000 ns MD simulation trajectories of SARS-CoV-2 PLpro complexes.

Figure 3: Number of contacts between residues of SARS-CoV-2 PLpro and bound ligands.

Click here to access/download;Figure;Figure 3 - PLPro contacts.tif ⬇



Figure 3: Number of contacts between residues of SARS-CoV-2 PLpro and bound ligands.

Figure 6: Inhibition of the SARS-CoV-2 PLpro protease and deubiquitinase activities by hypericin.